Title

A highly effective multi-string humidifier with a low gas stream pressure drop for desalination

Authors

Zeng, Zezhi
Sadeghpour, Abolfazl
Ju, Y Sungtaek

Publication Date

2019

DOI

10.1016/j.desal.2018.10.017

Peer reviewed

A HIGHLY EFFECTIVE MULTI-STRING HUMIDIFIER WITH A LOW GAS STREAM PRESSURE DROP FOR DESALINATION

Zezhi Zeng†*, Abolfazl Sadeghpour†, and Y. Sungtaek Ju

Department of Mechanical and Aerospace Engineering
University of California, Los Angeles, CA 90095, USA

ABSTRACT

The humidification-dehumidification (HDH) process is appealing for small-scale distributed desalination of high-salinity water. We report a new design of compact light-weight humidifiers with high effectiveness and low electric energy consumption for HDH systems. The new design consists of a dense array of vertically aligned strings, along which thin films of a heated liquid feed are allowed to flow under gravity. A counterflowing gas stream makes direct contact with liquid films carrying the generated water vapor to a dehumidifier. The unique geometric configuration of our design affords high interface-to-volume ratios necessary for high heat/mass exchange effectiveness and straight contiguous gas flow paths for reduced gas-phase pressure drops. We constructed a 0.4 m-tall prototype and examined the effects of the liquid flow rate, air velocity and feed liquid salinity on the heat/mass transfer performance and the gas stream axial pressure drop. Compared with previously reported pad humidifiers and spray columns, the present multi-string humidifier achieves almost 5 times the evaporation rate per humidifier volume at comparable gas stream pressure drops or an order of magnitude reduction in the gas stream pressure drop at comparable total evaporate rates. Our work demonstrates a highly-effective but compact and light-weight multi-string humidifier with a small gas stream axial pressure drop for HDH and related applications.

KEY WORDS: Direct-contact heat/mass exchanger, humidification-dehumidification, thermal desalination, humidifier

1. INTRODUCTION

Water is a precious and limited resource. Agriculture, drinking, sanitation and thermoelectric power plant cooling all require significant amounts of fresh water. However, 97% of water on earth is saline water and not suitable for many of these applications. This has motivated intense research efforts in developing various technologies for desalination and treatments/reuse of industrial and municipal waste water. The reverse osmosis (RO) [1, 2] has been widely used for desalination of sea water and treatment of certain waste water. Significant consumption of electricity, membrane fouling, and low limits on the acceptable salinity of feed water, however, have impeded their wider adoption [3]. Thermal desalination techniques, such as the multi-effect desalination (MED) and multi-stage flash desalination (MSF), can produce high quality distilled water [4]. However, relatively high total energy consumption and high capital/operating costs have presented barriers to their recent commercial deployments [5].

Humidification and dehumidification (HDH) is an intriguing thermal distillation technique for small-scale and mobile desalination and water treatment applications [6, 7] because it can operate under ambient pressure using low-grade and renewable heat sources and handle a wide variety of feed water streams. A HDH unit mimics natural water cycle by first humidifying a carrier gas and then condensing water vapor to produce distilled water.

Understanding the influence of various operating parameters (e.g., flow rates, inlet temperatures, and salinity) on the humidification process contributes significantly to the optimization of HDH systems. For example, a previous study [8] experimentally examined a pad humidifier and a tubular spray humidifier to determine how the seawater/air flow rate, seawater temperature and equipment dimension affect the evaporation rate. Another previous study [9] conducted a combined experimental and theoretical investigation of a pad humidifier used

†These authors contributed equally to this work
*Corresponding Author: zezhizeng@ucla.edu

in a multi-stage solar desalination unit. A multi-stage humidifier [10] was also reported to maximize the humidity ratio at the humidifier exit for increased fresh water production. There was also a study [11] where an experimental and modelling study was conducted to determine the mass transfer coefficient of both natural and forced convection in a vertical channel with parallel plates, which emulate structured-packing humidifiers. A related study [12] investigated how the salinity affects water evaporation rates and integrated the salinity into their empirical correlations for the flat plate humidifier.

With a growing concern over the global climate change, many previous studies explore the use of renewable energy sources, such as solar energy or geothermal energy, for powering HDH. One such study [13] constructed a thermodynamics model for a solar powered desalination unit and predicted that the water productivity in summer is twice larger than winter based on the solar radiation intensity data from Xi'an, China. A later study [14] constructed a large-scale pilot system with a 100 m^2 solar air heater field and demonstrated 1200 L/day fresh water production at an average solar radiation intensity of 550 W/m^2. Past studies [15] also successfully demonstrated utilization of geothermal energy for heat input.

Thermodynamically balancing the humidification and dehumidification processes in HDH systems helps effectively reduce overall entropy production and thereby improve the overall thermal efficiency of HDH processes [16, 17]. A parameter often used to quantify the performance of HDH systems is the gain output ratio (GOR), defined as the ratio between the latent heat of evaporation and the net thermal energy input. Previous studies performed thermodynamic optimization analyses to explore ways to improve the GOR of HDH systems [18–20].

Past studies [21], for example, aimed to optimize extractions and subsequent injections of a humidified gas between a humidifier and a dehumidifier and experimentally demonstrated that a single extraction-injection step could improve GOR from 2.6 to 4 using a commercial packed bed humidifier and a shell-and-tube exchanger dehumidifier. Theoretical analyses, indeed, projected that GOR values greater than 10 are possible by integrating multiple extraction/injection steps.

Such high values of GOR, however, were achievable only for humidifiers and dehumidifiers with correspondingly high heat/mass exchange effectiveness. In other words, a critical challenge is often not whether one can achieve high GOR values using a given humidifier or dehumidifier design concept. A bigger challenge arises from the fact that existing design concepts would require very large and/or heavy units with high capital and installation costs or compact units with very high pressure drops and hence high operating costs.

Conventional shell and tube exchangers [22, 23] are typically heavy and expensive and suffer from problems of corrosion and scaling. Direct-contact heat/mass exchangers help avoid the latter problems by suppressing phase change on solid surfaces and offer high specific interface areas for heat/mass transfer [24]. Recent studies reported the use of bubble columns as humidifiers or dehumidifiers [25–27]. A stream of air injected to a pool of water through small holes can create large liquid-gas interfacial areas for effective heat and mass transfer. A past study [28] experimentally investigated the effects of water temperature, hole diameter, and air flow rate on the performance of a bubble column humidifier. However, bubble columns introduce significant gas-stream pressure drops and thereby require high electric energy consumption.

To tackle these challenges, we report a new design for humidifiers in the form of a multi-string heat/mass exchanger. The multi-string humidifier consists of a dense array of vertical aligned strings as illustrated in Fig. 1. A heated liquid feed stream is flown down the strings while making direct contact with a counterflowing gas stream that carries the evaporated water. The unique configuration of our multi-string humidifier design affords high interface-to-volume ratios necessary for high heat/mass exchanger effectiveness in a compact and light-weight unit and at very low gas-stream pressure drops.

A previous study using a non-volatile liquid as a working fluid demonstrated that a direct-contact heat exchanger of the same geometric design can deliver the same heat transfer effectiveness at a much lower pressure drop than traditional parallel-plate structured packings [29, 30]. Earlier studies of multi-string exchangers also suggested their applications in CO_2 absorption and hydrazine vapor separation [31–33].

In the present work, we report a combined experimental characterization and modeling study to validate our humidifier design, specifically with desalination applications in mind. The effects of the liquid flow rate, air velocity, and liquid salinity on the heat and mass transfer rates are experimentally characterized. The mass transfer conductance-interfacial area products obtained are next used to quantify the performance of a multi-string humidifier. The gas-stream pressure drop of the multi-string humidifier is also measured and compared with existing humidifier designs.

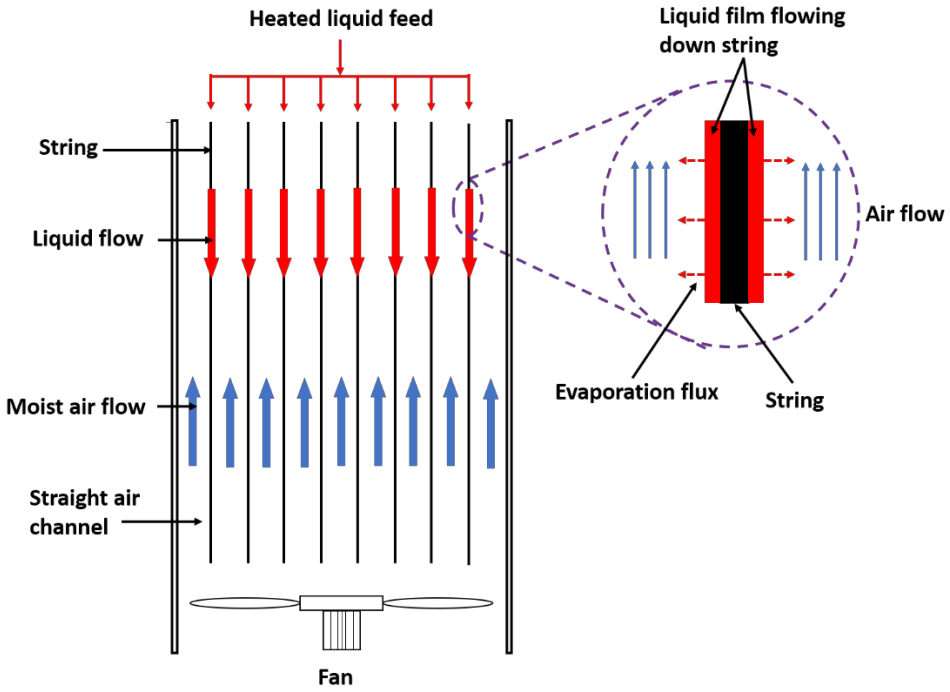

Fig. 1 Schematic illustrating the operation of a multi-string humidifier.

2. EXPERIMENTAL

A schematic of the experimental setup used in the present study is shown in Fig. 2. The setup consists of a vertical acrylic cylindrical pipe of an inner diameter 6.35 cm for air flow; a top liquid reservoir; a bottom chamber with flow conditioners to ensure a uniform inlet air stream; and a square array of 24 cotton strings (R_w = 0.375 mm). The top view of the string array is shown in Fig. 3. The string pitch used in the current study is 10 mm. All the strings are fixed to a metal rod to keep them under tension.

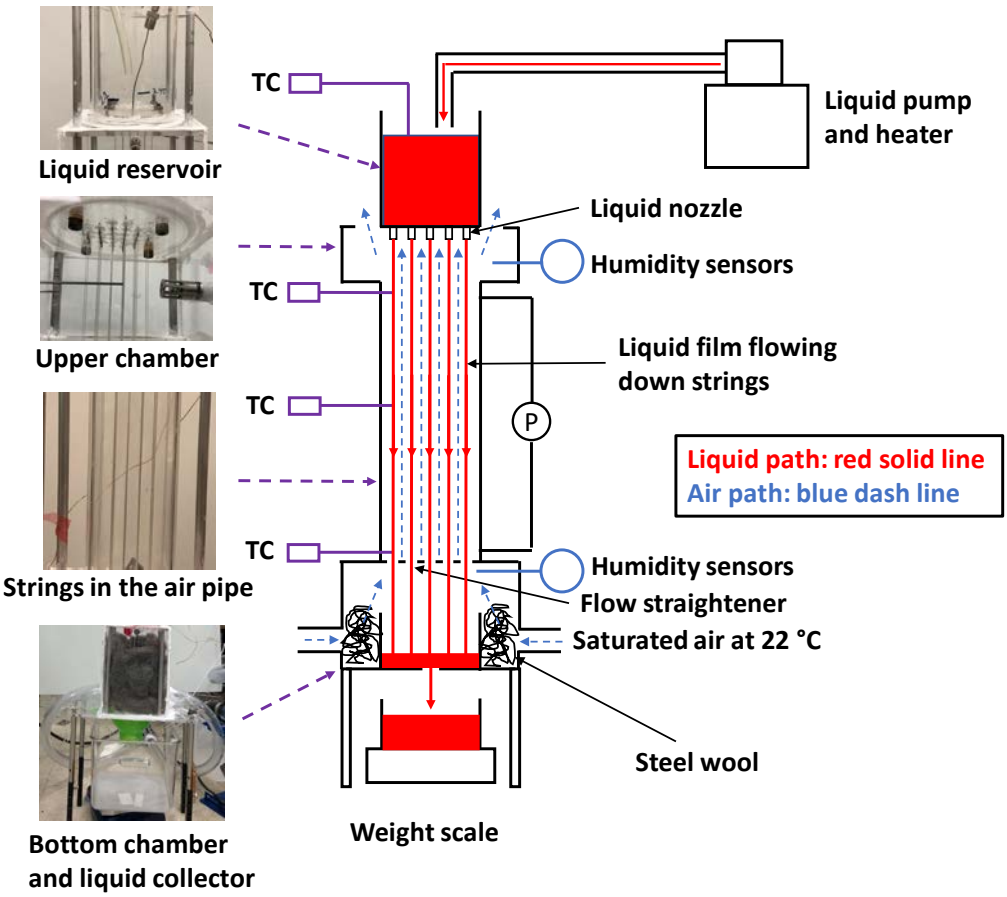

Fig. 2 Schematic of the experimental setup used to characterize the heat/mass transfer and air-stream pressure drop in the multi-string humidifier.

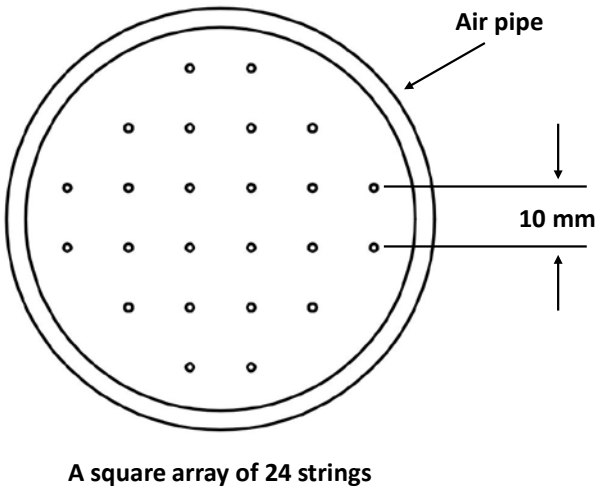

Fig. 3 Top view of a square array of 24 strings. The string pitch used for the experimental results reported in the article is 10 mm.

A bath circulator is used to heat the feed water and pump it into the top reservoir. The heated liquid is divided into multiple streams using an array of nozzles built into the top reservoir. As the liquid streams flow down

the strings under gravity, they form traveling liquid beads due to intrinsic instability caused by interplay among surface tension, viscous, gravity, and inertia forces [34].

The liquid is then collected in a bottom reservoir, whose weight is monitored using a weight scale to determine the liquid flow rate. A converging cone is used to facilitate the collection of the liquid. A stream of air, saturated with water at 22 °C (relative humidity = 100%), is introduced into the bottom of the main section to mimic a closed-air open-water HDH cycle. A steel wool is used to homogenize the air flow. A flow straightener is placed at the inlet of the test section to ensure a uniform inlet air stream. The gas flow rate is measured using a variable-area flow meter with a range of 0.8 - 8 SCFM.

The spatial temperature distributions of the liquid film and the air stream are measured using micro-thermocouples with a tip diameter of 250 μm. Three pairs of micro-thermocouples are placed at three axial locations (0.1 m, 0.25 m, and 0.4 m) from the liquid nozzle, each at one of two different radial locations (i.e. next to 2 different strings), as shown in Fig. 2 to measure local liquid temperatures. We place the micro-thermocouples nominally 0.1 mm away from dry strings such that the micro-thermocouples are fully immersed in liquid films without actually touching the string. One thermocouple is placed inside the top liquid reservoir to monitor the liquid inlet temperature.

To measure the air stream temperatures, we place six additional micro-thermocouples at three axial locations (0 m, 0.25 m, and 0.4 m), one group along the test section center and the other group near the test section boundary. Two humidity sensors are used to monitor the gas stream humidity at the air inlet and the air outlet. Pressure transducers are installed at two axial locations 0.3 m apart to measure the gas-stream pressure drops.

Feed water streams at three different salinity levels are examined in the present study. They are the distilled water, the water with a salinity of 35 g/kg, and the water with a salinity of 108 g/kg, respectively.

For each experimental run, the liquid and air flow rates are first adjusted to their respective set values. The measurements are taken after readings from all the thermocouples and pressure transducers are stabilized to within 1% over a 15-minute period. Each experimental run lasted for two minutes. A sampling frequency of 50 Hz is used for the thermocouples. At each liquid and air flow rate combination, experiments are repeated at least three times to confirm that the data are reproducible to within 5%. The liquid flow rates examined in the current study range from 0.7 to 3.6 g/s. The volumetric flow rates of the air stream vary from 1 to 6 SCFM.

Estimated uncertainty in thermocouple readings is ± 0.1 °C. Radial variations in the liquid temperature across the test section, which may be attributed to slight differences in the liquid flow rate among the strings, is estimated to be ± 2 °C. Radial variation in the air temperature at a given axial location is estimated to be ± 1 °C. Uncertainty in the measured air velocities is estimated to be 0.05 m/s, uncertainty in the measured liquid flow rates 0.1 g/s, uncertainty in the measured pressure drops 0.05 Pa, and uncertainty in the relative humidity values 2%.

3. THEORETICAL ANALYSIS

To help interpret the experimental data, we construct a steady-state model based on the mass and energy balance following a previous study [35]:

$$\frac{d\dot{m}_{\mathrm{L}}}{dA_z} = \frac{d\dot{m}_{\mathrm{G}}}{dA_z} \tag{1}$$

$$\frac{d}{dA_z}(\dot{m}_{\mathrm{L}} h_{\mathrm{L}}) = \frac{d}{dA_z}(\dot{m}_{\mathrm{G}} h_{\mathrm{G}}) \tag{2}$$

Here $\dot{m}_{\mathrm{L}}$ and h_L denote the mass flow rate and enthalpy of the liquid, respectively. The symbols $\dot{m}_{\mathrm{G}}$ and h_G denote the mass flow rate and enthalpy of the air. The cumulative liquid-gas interfacial area, which increases linearly from the liquid nozzle as we move downstream, is labeled A_z.

High rates of evaporation can lead to a non-negligible normal velocity component of water vapor near the surface of water (Fig. 4). This so-called convective component is suggested to be significant [35] when the water temperature exceeds approximately 50 °C

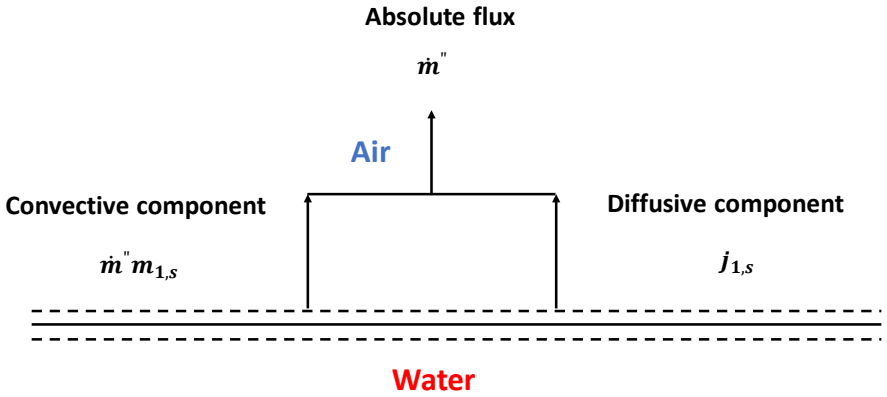

Fig. 4 The convective and diffusive components of the absolute flux [35]

One writes the absolute flux of water vapor from the water surface $\dot{m}''$ as

$$\dot{m}'' = m_{1,s}\dot{m}'' + j_{1,s} = m_{1,s}\dot{m}'' - \rho D_{12}\frac{dm_1}{dr}. \tag{3}$$

Here, $j_{1,s}$ is the diffusive component of the mass flux, m_1 is the mass fraction of water, D_{12} is the water vapor-air diffusion coefficient, and ρ is the vapor density. The subscript s denotes the properties at the water surface and the subscript e denotes those in the gas stream.

After rearranging and integrating the equation across the boundary layer of width δ, we obtain

$$\int_{m_{1,s}}^{m_{1,e}} \frac{dm_1}{m_1\dot{m}'' - \dot{m}''} = \int_0^{\delta} \frac{\dot{m}'' dr}{\rho D_{12}}, \tag{4}$$

and

$$\frac{m_{1,e}-1}{m_{1,s}-1} = \exp\left(\frac{\dot{m}''\delta}{\rho D_{12}}\right). \tag{5}$$

We rewrite Equation (5) for later convenience as

$$1 + \frac{m_{1,s}-m_{1,e}}{1-m_{1,s}} = \exp\left(\frac{\dot{m}''\delta}{\rho D_{12}}\right). \tag{6}$$

Solving Eq. (6) for $\dot{m}''$ and using the mass transfer driving force B_{m1} defined as

$$B_{m1} = \frac{m_{1,s}-m_{1,e}}{1-m_{1,s}}, \tag{7}$$

we obtain

$$\dot{m}'' = \frac{\rho D_{12}}{\delta}\ln(1 + B_{m1}) = \frac{\rho D_{12}}{\delta}\frac{\ln(1+B_{m1})}{B_{m1}}B_{m1}. \tag{8}$$

Using the mass transfer conductance g_m^* defined as $\rho D_{12}/\delta$, we finally write

$$\frac{d\dot{m}_L}{dA_z} = \dot{m}'' = g_m^* \frac{\ln(1+B_{m1})}{B_{m1}} B_{m1}. \quad (9)$$

We rewrite the energy balance equation by substituting the total evaporation rate in Eq. (2). The total energy transfer from liquid film to air stream includes both energy transfer from force convection and evaporation:

$$\frac{d}{dA_z}(\dot{m}_L h_L) = q_{conv} + q_{evap} \quad (10)$$

$$q_{evap} = g_m^* \frac{\ln(1+B_{m1})}{B_{m1}} B_{m1} h_{1,s} \quad (11)$$

$$q_{conv} = g_h C_{p,G}(T_L - T_G) \quad (12)$$

Here, q_{conv} and q_{evap} denote the convective and evaporative heat flux, respectively. $h_{1,s}$ accounts for both the latent heat and the enthalpy variation due to temperature change. $C_{p,G}$ is the air heat capacity. We estimate the heat transfer conductance using the heat and mass transfer analogy [35, 36]:

$$\frac{g_m^*}{g_h} = (Le)^{\frac{2}{3}} \approx 1.08 \quad (13)$$

The relative humidity of air is measured to be 100% at both the inlet and the outlet of our setup for all experimental conditions reported in the article. The properties of pure water and saturated air are obtained from existing literatures [37–40]. The latent heat and the specific enthalpy of the saline water are calculated from

$$h_{fg,sw} = h_{fg,w}(1 - S), \quad (14)$$

and

$$h_{sw} = h_w - S(a_1 + a_2 S + a_3 S^2 + a_4 S^3 + a_5 t + a_6 t^2 + a_7 t^3 + a_8 S t + a_9 S^2 t + a_{10} S t^2). \quad (15)$$

The coefficients are listed below:

$$a_1 = -2.348 \times 10^4, a_2 = 3.152 \times 10^5, a_3 = 2.803 \times 10^6, a_4 = -1.446 \times 10^7, a_5 = 7.826 \times 10^3,$$
$$a_6 = -4.417 \times 10^1, a_7 = 2.139 \times 10^{-1}, a_8 = -1.991 \times 10^4, a_9 = 2.778 \times 10^4, a_{10} = 9.728 \times 10^1$$

Here, $h_{fg,sw}$ and $h_{fg,w}$ denote the latent heat of saline water and pure water in J/kg, respectively. h_{sw} and h_w are the enthalpy of saline water and pure water, respectively, in J/kg, S the salinity in kg/kg, and t the temperature in °C. The vapor pressure of saline water is estimated using Raoult's correlation:

$$\frac{P_{v,w}}{P_{v,sw}} = 1 + 0.57357 \times \left(\frac{S}{1-S}\right) \quad (16)$$

$P_{v,w}$ and $P_{v,sw}$ represent the vapor pressure of pure water and saline water, respectively.

The only unknown parameter in this model is g_m^*. We iteratively solve Eqs. (1) and (2) numerically, while treating g_m^* as the adjustable fitting parameter, until the calculated spatial temperature profile fits the experimental data. Linear temperature profiles based on the inlet and outlet temperatures are used as initial guesses for the liquid and air stream. The extracted value of g_m^* is then considered to be the overall mass transfer conductance. A typical fit is shown in Fig. 5.

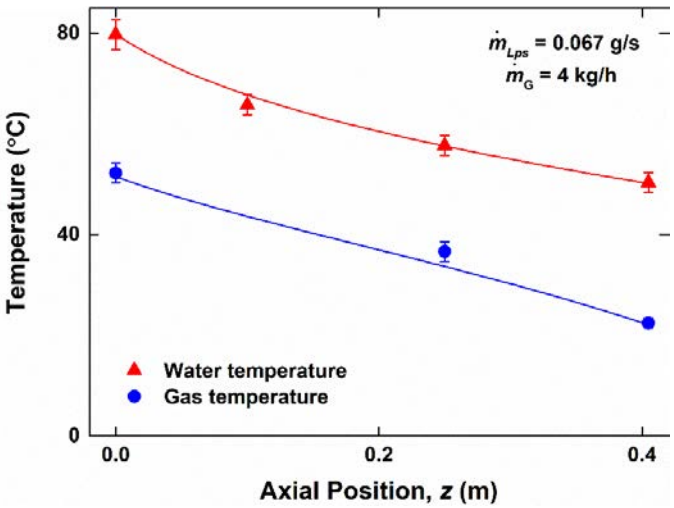

Fig. 5 A representative fit of the experimentally measured spatial profiles of the liquid and air temperature using the heat/mass transfer model.

Following the convention for humidifiers in the literature, we report the total air flow rates. The superficial air velocity can be calculated from the total air flow rate by dividing them with the cross-sectional area of the acrylic pipe (3.16×10^{-3} m^2). A mass flow rate of 4 kg/h, for example, corresponds to a superficial air velocity of 0.3 m/s. The liquid flow rate is reported as the liquid flow rate per string, $\dot{m}_{\mathrm{Lps}}$. The corresponding total liquid mass flow rate is $\dot{m}_{\mathrm{L}}$ can be calculated by multiplying $\dot{m}_{\mathrm{Lps}}$ with the total number of the strings 24.

4. RESULTS AND DISCUSSION

4.1 Mass transfer conductance

We first examine the extracted values of the mass transfer conductance g_{m}^* to elucidate the effects of the liquid flow rate, air flow rate, and salinity. Following a previous study [31], we define the overall capacity coefficient as $g_{\mathrm{m}}^* A/V$. Here, A and V denote the liquid-gas interfacial area and the volume of the humidifier, respectively. This parameter essentially helps quantify the mass transfer rate per unit volume of a humidifier.

Figure 6a shows that the overall capacity coefficient increases approximately linearly with the air flow rate. Differences in the overall capacity coefficients are within 10% for liquid streams of the three different salinities tested. In contrast, Figure 6b shows that the overall capacity coefficient increases as the liquid flow rate per string increases. Both results are consistent with the observed liquid film profiles shown in Fig. 7.

Because the salinities used are not high enough to significantly alter the surface tension, viscosity or density, the liquid films of the three different salinities show very similar liquid film profiles. We remind the reader that the intrinsic instability of liquid films flowing down vertical strings result in the formation of traveling liquid beads. For a given liquid flow rate (either Fig. 7a or Fig. 7b), the liquid bead sizes and the inter-bead spacings are within 2% of each other. In contrast, when the liquid flow rate is changed, the inter-bead spacing also changes. As the liquid bead size is approximately constant, to accommodate a higher mass flow rate, the inter-bead spacing needs to decrease [34]. That is, per unit volume, there are more liquid beads that facilitate mass transfer accompanying evaporation or condensation [41] with their localized curved interfaces. The overall capacity coefficient therefore increases with increasing liquid mass flow rates.

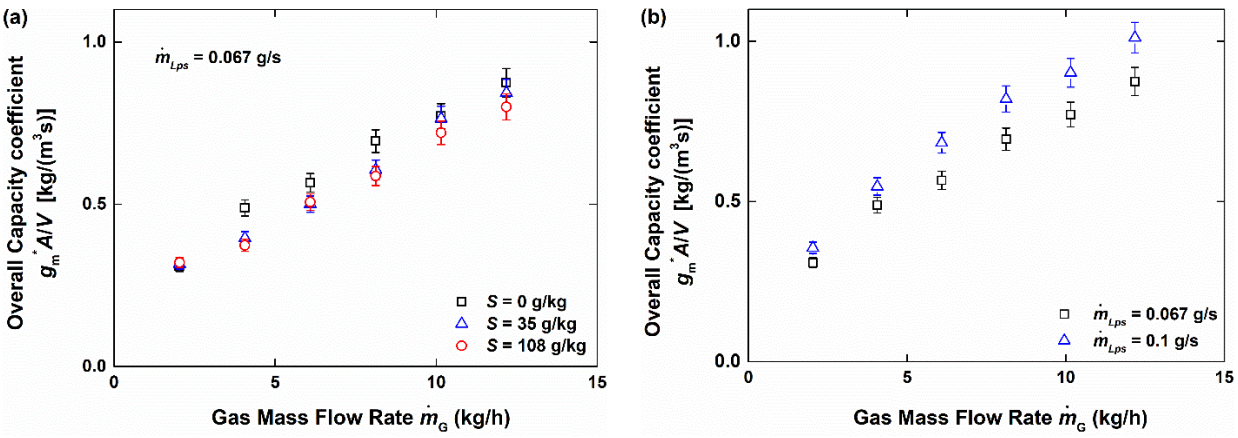

Fig. 6 Overall capacity coefficients for the feed water streams of (a) three different salinities at a fixed liquid flow rate. (b) two different liquid flow rates at a fixed salinity. The inlet liquid and air temperatures are 80 ºC and 22 ºC, respectively. Air flow rates of 0 - 15 kg/h correspond to superficial air velocities of 0 – 1.1 m/s.

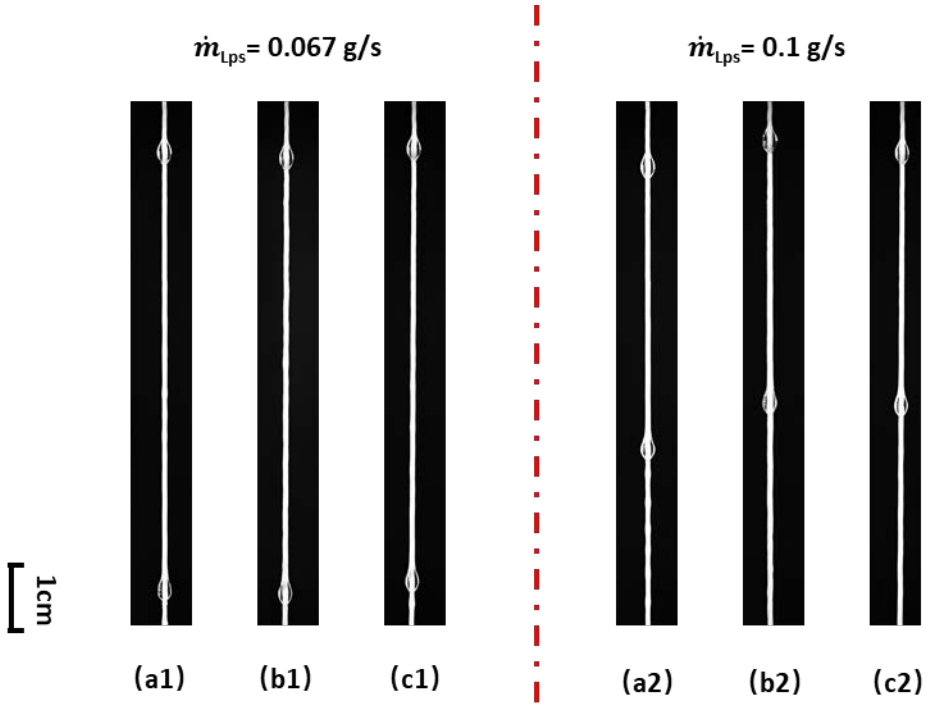

Fig. 7 Liquid film profiles at two different liquid flow rates ($\dot{m}_{Lps}$ = 0.067 or 0.1 g/s) for liquid feed streams of three different salinities: (a) S = 0 g/kg (b) S = 35 g/kg (c) S = 108 g/kg.

4.2 Evaporation rate and humidifier effectiveness

The best fit value of g_m^* is then used to compute the total evaporation rate shown in Fig. 8 using two methods to confirm the consistency of the model. In the first method, we numerically integrate Eq. (9) along the axial direction while approximating the liquid film as a smooth cylindrical surface of radius obtained from the Nusselt solution [42]. In the second method, we calculate the evaporation rate from a difference in the liquid mass flow rate $\dot{m}_L$ between the inlet and the outlet. We confirm that the two methods yield the same values of the total evaporation rate.

Figure 8 shows the obtained evaporation rates for feed streams with the three different salinities at a fixed liquid flow rate. Although the mass transfer conductance values are similar, the streams with higher salinity values yields slightly (5~ 10%) lower evaporation rates because of lower water vapor pressures, consistent with the results from previous studies [8, 12]. The lower vapor pressures lead to lower convective components of the absolute fluxes. Although the mass transfer conductance shows the same value, the total evaporation rate is affected by salinity because of different convective components.

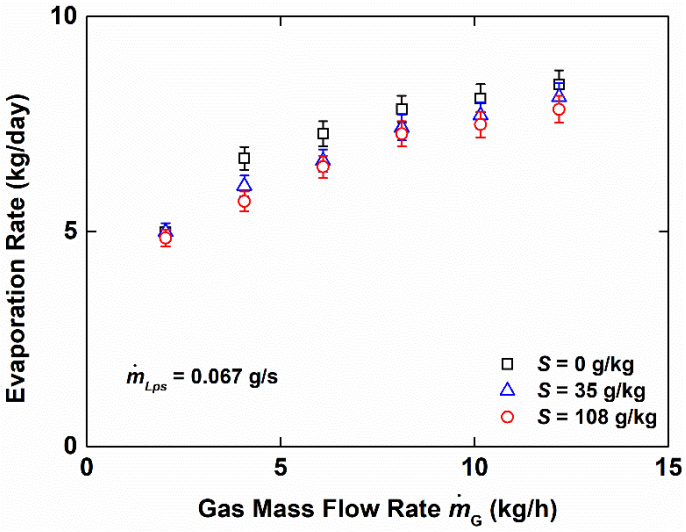

Fig. 8 The water evaporation rate as a function of the air mass flow rate for liquid feed streams with three different salinities. The inlet liquid and air temperature are fixed at 80 ºC and 22 ºC, respectively.

We next normalize the water evaporation rate with the feed water flow rate (Eq. 17) to examine the influence of the liquid flow rate on the evaporation rate. The normalized evaporation rate is identical to the maximum water recovery ratio (RR) when one assumes that the water vapor completely condenses in a dehumidifier.

$$\beta = \frac{\dot{m}_{\mathrm{L,in}} - \dot{m}_{\mathrm{L,out}}}{\dot{m}_{\mathrm{L,in}}} \tag{17}$$

Figure 9a shows that the higher liquid flow rate leads to the higher evaporation rate. This is consistent with the increase in the overall capacity coefficient, which results largely from the decreased inter-bead spacing, as discussed in Sec 4.1. However, the normalized evaporation rate is smaller for the higher liquid flow rate (Fig. 9b). This suggests that the enhancement in heat/mass transfer rates due to decreasing inter-bead spacing is not sufficient to fully counteract an increase in the liquid mass flow rate.

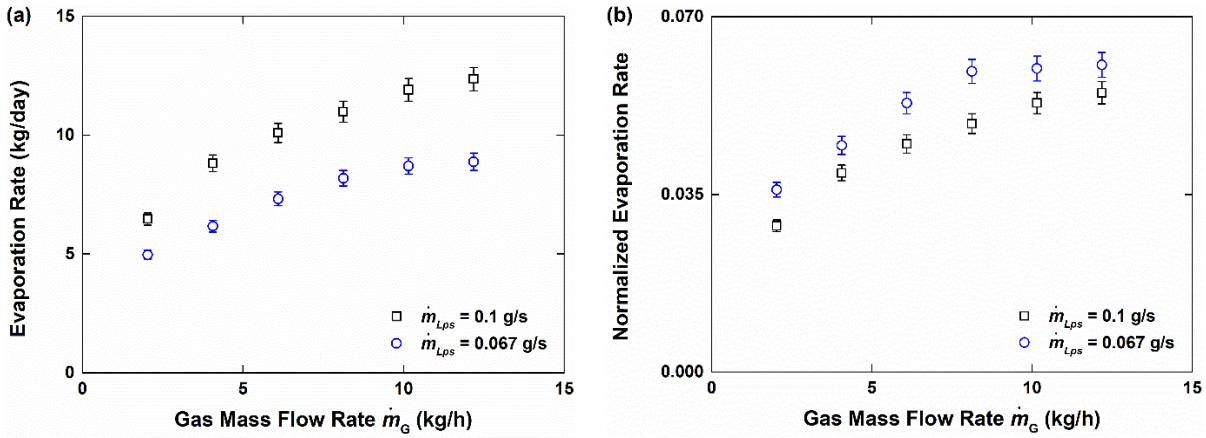

Fig. 9 (a) The calculated evaporation rate as a function of the air mass flow rate for two different liquid flow rates. (b) The corresponding normalized evaporation rate as a function of the air mass flow rate. Distilled water is considered as the feed liquid. The inlet liquid and air inlet temperature are fixed at 80 ºC and 22 ºC, respectively.

The humidifier effectiveness is often defined as the ratio of the change in the real enthalpy to the maximum possible change in the liquid enthalpy [43]:

$$\varepsilon = \frac{\Delta H}{\Delta H_{\max}} \tag{18}$$

Here, ΔH denotes the enthalpy change of either the cold stream or the hot stream. $\Delta H_{\max}$ represents the maximum possible enthalpy change. Under the experimental conditions used in the present study, the maximum possible enthalpy change is that for the liquid stream.

Taking the ratio between the humidifier effectiveness and the normalized evaporation rate, we obtain

$$\frac{\varepsilon}{\beta} = \frac{\Delta H}{\Delta H_{\max}\,\beta} = \frac{h_{\mathrm{L,in}} - h_{\mathrm{L,out}}}{\Delta h_{\max}} \frac{\dot{m}_{\mathrm{L,in}}}{\dot{m}_{\mathrm{L,in}} - \dot{m}_{\mathrm{L,out}}} = \frac{(\dot{m}_{\mathrm{L,in}} - \dot{m}_{\mathrm{L,out}})\Delta h_L}{(\dot{m}_{\mathrm{L,in}} - \dot{m}_{\mathrm{L,out}})\Delta h_{\max}} = \frac{\Delta h_L}{\Delta h_{\max}} \tag{19}$$

Here, $h_{\mathrm{L,in}}$ and $h_{\mathrm{L,out}}$ denote the total specific enthalpy of the liquid at the inlet and the outlet, respectively. $\Delta h_{\max}$ is the difference between the total specific enthalpy at the liquid inlet temperature and the total specific enthalpy at the air inlet temperature. Since the latent heat dominates the total specific enthalpy, Δh_{L} varies by only 2% from 20 ºC to 90 ºC. $\Delta h_{,\max}$ is only a function of the liquid and air inlet temperatures. As a result, the normalized evaporation rate and the humidifier effectiveness depend linearly on each other for given liquid and gas inlet temperatures.

For one pair of the liquid inlet temperature and the air inlet temperature, we perform experiments with different combinations of liquid flow rates and air velocities. Figure 10 shows the relationship between the humidifier effectiveness and the normalized evaporation rate thus obtained. The experimental results agree with the analytical prediction to within 5%, confirming that the normalized evaporation rate is thermodynamically limited by the liquid and gas inlet conditions.

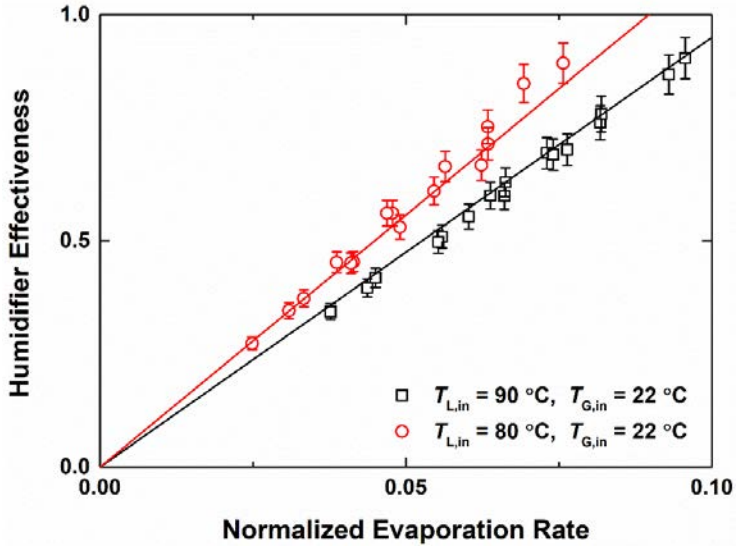

Fig. 10 The relationship between the humidifier effectiveness and the normalized evaporation rate. The symbols are the experimental data and the solid lines are the prediction from Eq. (19).

4.3 Gas stream pressure drop

The overall pressure drop in the gas stream may be divided into two components: the frictional pressure drop P_f and the acceleration pressure drop due to evaporation P_e [23]:

$$\Delta P = \int_0^L \left(\frac{dP_f}{dz} + \frac{dP_e}{dz}\right) dz \tag{20}$$

Under the experimental conditions used in the present study, the gas streams are expected to be in the turbulent regime. For turbulent flows along an infinitely long rod bundles, previous studies [44–46] reported engineering correlations for the friction loss. These correlations present the friction factor in terms of a geometric parameter defined in Eq. 21. The geometric parameter is defined using an equivalent annular zone of radius r_0, which has the same area as a square unit cell around each string [44], and the radius of the cylindrical liquid film around strings, r_1 as shown in Fig. 11.

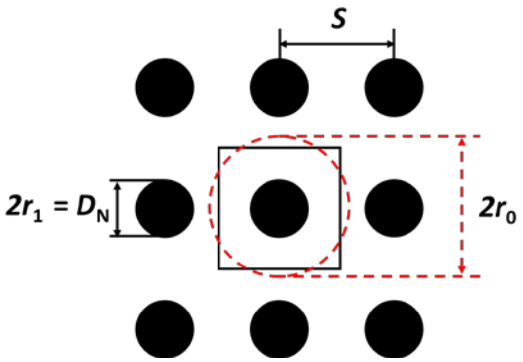

Fig. 11 The geometric parameters of a square array of strings. The red circle represents the equivalent annual zone of a unit square cell (the black square).

The geometric parameter x [44] is defined as

$$x = \frac{r_0}{r_1} = \sqrt{\frac{4}{\pi}}\,\frac{s}{D_N} \tag{21}$$

Here D_N and s represent the average liquid film diameter calculated from the Nusselt solution [42], and the string pitch, respectively.

The universal velocity profile for turbulent flows on circular tubes was taken as [47]

$$u^+ = 2.5 \ln y^+ + 5.5 \tag{22}$$

Here, $u^+ = u/u^*$ is the dimensionless velocity, $u^*=\sqrt{(\tau_w/\rho)}$ is the frictional velocity, $y^+ = \rho y u^*/\mu$ is the dimensionless distance from the wall. An engineering correlation for the friction factor f_T of an annular zone in the turbulent regime was reported in terms of the frictional velocity as [48]

$$\sqrt{\frac{8}{f_T}} = 2.5 \ln\left(\frac{\rho L u^*}{\mu}\right) + 5.5 - \frac{3.966+1.25x}{1+x} \tag{23}$$

Here, $L = r_0 - r_1$ is the width of the annular zone. The shear stress τ_w can be expressed as $f_T \rho u^2/8$. Eq. (23) can then be re-written as

$$\sqrt{\frac{8}{f_T}} = 2.5 \ln\left(\frac{\rho (r_0-r_1) u}{\mu} \sqrt{\frac{f_T}{8}}\right) + 5.5 - \frac{3.966+1.25x}{1+x} \tag{24}$$

The Reynolds number of the equivalent annular zone is defined as $Re = \rho u D_h/\mu$, where D_h is the hydraulic diameter and equal to $2(r_0^2 - r_1^2)/r_1$. A more commonly used form of Eq. (24) can be obtained by substituting this definition of the Reynolds number into Eq. (24) and rearranging the resulting equation:

$$\sqrt{\frac{8}{f_T}} = 2.5 \ln\left(Re \sqrt{\frac{f_T}{8}}\right) + 5.5 - \frac{3.966+1.25x}{1+x} - 2.5 \ln(2 + 2x) \tag{25}$$

The frictional pressure drop is obtained from

$$\frac{\Delta P_f}{\Delta z} = \frac{f_T \rho u^2}{2 D_h} \tag{26}$$

The acceleration pressure drop due to evaporation is calculated from [23]

$$\frac{dP_e}{dz} = \left(\frac{\dot{m}_G}{A_C}\right)^2 \left(\frac{1}{\rho_G} - \frac{1}{\rho_f}\right) \frac{d\omega}{dz} \tag{27}$$

Here, A_c denotes the air stream cross-sectional area, ρ_G the air density, ρ_f the water density, and ω the humidity ratio. The relative humidity values of the air stream at the inlet and outlet are experimentally determined to be 100%. The air inlet temperature is fixed at 22 °C and the corresponding humidity ratio is 16.74 g water/kg dry air. The outlet air temperature varies with different experimental conditions (liquid mass flow rates, liquid inlet temperatures, and air mass flow rates). The corresponding humidity ratio can be obtained from the thermodynamics table [37–40]. The humidity ratio can also be related to the mass fraction by $\omega = m_1/(1 - m_1)$.

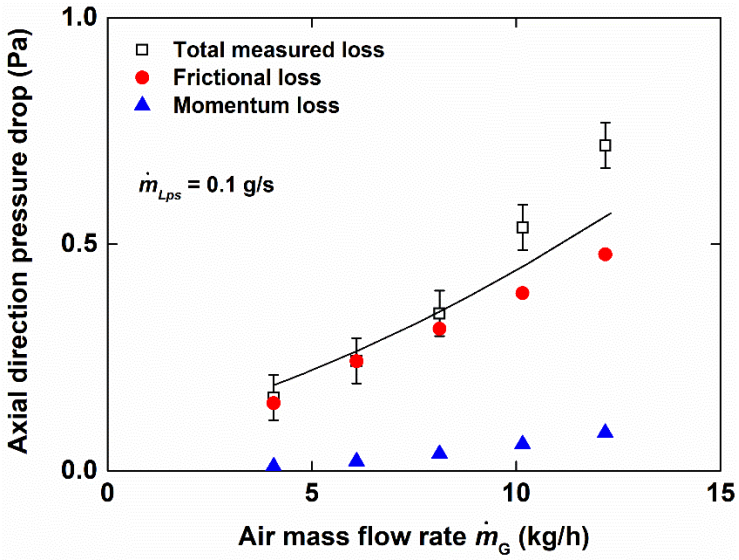

Fig. 12 The pressure drop along the gas stream of the multi-string humidifier. The squares are the experimental data. The line represents prediction from Eq. (20). The circles and triangles show the two components of the pressure drop. The air flow rates of 0 - 15 kg/h correspond to the superficial air velocities of 0 – 1.1 m/s.

Figure 12 shows the measured and predicted axial pressure drop in the gas stream as a function of the gas mass flow rate. Note first that the gas stream pressure drop is very small, only of the order of 1 Pa. The model prediction agrees with the experimental data to within 5% for air mass flow rates below 10 kg/h. But the model underpredicts the pressure drops by as much as 20% at higher air velocities. This is in part due to the additional form drag caused by liquid beads traveling down the strings (see Fig. 7) [29], which is not accounted for in the engineering correlation for smooth rod bundles. The acceleration pressure drop due to evaporation contributes 10 - 15% of the total pressure drop at mass flow rates higher than 10 kg/h where evaporation rate is correspondingly higher.

Smaller string pitches lead to higher values of the overall capacity coefficient, $g_m^* A/V$, but at the expense of increased gas-stream pressure drops. The smallest practical string pitch is estimated to be of the order of 5 mm, constrained in part by liquid flooding at the air inlet and in part by interference between liquid films flowing down adjacent strings. All the data reported in the present manuscript is based on a string array of pitch 10 mm as a compromise between achieving a high overall capacity coefficient and achieving a low gas-stream pressure drop. In separate unreported experiments, we used string arrays with pitches as big as 20 mm and arrays with pitches as small as 5 mm. The smallest pitch presented many practical challenges in manufacturing and assembly. We observed almost 4 times increase in the overall capacity coefficient but also a commensurate increase in the air stream pressure drop. The results were consistent with our model predictions.

Popular string arrangements are square and triangular arrays. Previous study [49] showed that the friction factor for flows along a triangular array of rods is higher than along a square array for the same porosity. But the difference falls below 2% when porosity values are higher than 0.95 [49], which is expected to be the case in our multi-string humidifiers. We therefore expect the string array arrangement to have a small influence on the gas-stream pressure drop and evaporation rate for a given string pitch and a porosity.

4.4 Humidifier performance comparison

We lastly compare the performance metrics of our multi-string humidifier with other types of previously reported humidifiers [8]: a pad humidifier and a spray humidifier. The present multi-string humidifier has a height of 0.4 m and a cross-sectional area of 0.0032 m^2. The pad humidifier was made of a corrugated cellulosic material similar to packed beds and used widely in humidifiers in HDH systems [8, 13, 14]. The pad humidifier reported in a previous study has a height of 0.332 m and a cross-sectional area of 0.25 m^2 [8]. The spray humidifier consisted of four polypropylene nozzles spraying seawater into a counterflowing air stream. The spray humidifier had a height of 2 m and a cross-sectional area of 0.07 m^2.

We compare the daily water evaporation rates per unit humidifier volume as one main performance metric. In the comparison, we selected the experiments where the superficial air velocities were approximately the same. But the superficial liquid velocities differed slightly: 0.6 mm/s for our multi-string humidifier; 0.65 mm/s for the pad humidifier; and 1.41 mm/s for the spray humidifier.

Figure 13 shows that the present multi-string humidifier can achieve higher evaporation rates at much lower gas stream pressure drops. This is attributed to the unique geometric configuration of our multi-string humidifier that offers high interfacial areas per unit volume while providing straight and contiguous gas flow paths.

A bubble column is another widely used device configuration for humidification. However, the working mechanism of bubble columns is rather different from counterflow exchangers, making direct comparison difficult. Previously reported bubble column humidifiers achieved evaporation rates of approximately 5000-8000 kg/day/m^3 at gas stream pressure drops higher than 10 kPa [27]. As a conservative estimate, only the volume of the water reservoir is considered as the volume of the bubble columns.

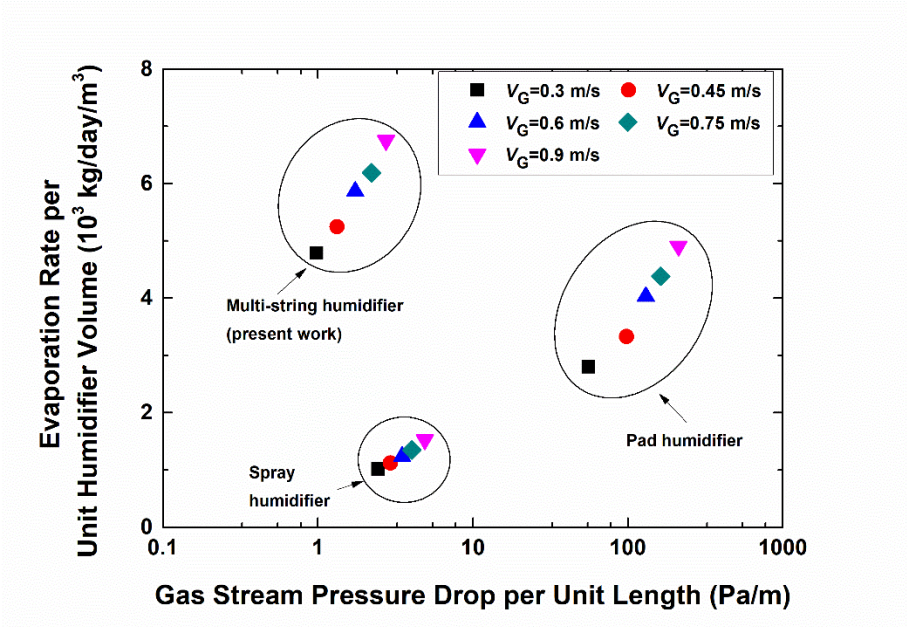

Fig. 13 The comparison of the performance of the present multi-string humidifier with other types of humidifiers [8].

5. CONCLUSIONS

A new design of humidifiers consisting of a dense array of strings for humidification-dehumidification desalination is presented and experimentally investigated in this study. We show that this new design enables humidifiers to achieve high heat and mass transfer rates without suffering from a large gas-stream frictional loss. We extract the overall capacity coefficient from measured spatial temperature profiles to quantify the

humidifier performance. The overall capacity coefficient increases with increasing liquid and air flow rates but varies within 10% for feed streams with salinities ranging from 0 to 108 g/kg. The saline water with the highest salinity used delivers approximately 10% lower evaporation rates due to its lower water vapor pressures. The multi-string humidifier can deliver comparable evaporation rates at an order of magnitude gas phase pressure drop than a pad humidifier or 5 times higher evaporation rates at a comparable gas phase pressure drop than a spray humidifier. The present study demonstrates a multi-string humidifier with superior performance for potential applications in small-scale and mobile desalination.

While the present article focuses exclusively on humidification, we recognize that it represents half of the humidification-dehumidification system. There also exists a pressing need for further innovations in heat and mass exchanger technologies for dehumidification. Balancing as well as optimizing the performance of humidifiers and dehumidifiers is critical to enhancing the overall system-level energy efficiency of integrated humidification-dehumidification systems.

ACKNOWLEDGMENT

The present article is based on work supported in part by the National Science Foundation through grant CBET-1358034 and the Simons Foundation Math+X Investigator Award 510776.

REFERENCES

[1] K. P. Lee, T. C. Arnot, and D. Mattia, "A review of reverse osmosis membrane materials for desalination—development to date and future potential," *J. Membr. Sci.*, vol. 370, no. 1–2, pp. 1–22, 2011.

[2] G. Kang and Y. Cao, "Development of antifouling reverse osmosis membranes for water treatment: A review," *Water Res.*, vol. 46, no. 3, pp. 584–600, Mar. 2012.

[3] M. F. A. Goosen, S. S. Sablani, H. Al-Hinai, S. Al-Obeidani, R. Al-Belushi, and aD Jackson, "Fouling of reverse osmosis and ultrafiltration membranes: a critical review," *Sep. Sci. Technol.*, vol. 39, no. 10, pp. 2261–2297, 2005.

[4] A. D. Khawaji, I. K. Kutubkhanah, and J.-M. Wie, "Advances in seawater desalination technologies," *Desalination*, vol. 221, no. 1, pp. 47–69, Mar. 2008.

[5] I. S. Al-Mutaz, "A comparative study of RO and MSF desalination plants," *Desalination*, vol. 106, no. 1, pp. 99–106, Aug. 1996.

[6] A. Giwa, N. Akther, A. A. Housani, S. Haris, and S. W. Hasan, "Recent advances in humidification dehumidification (HDH) desalination processes: Improved designs and productivity," *Renew. Sustain. Energy Rev.*, vol. 57, pp. 929–944, May 2016.

[7] S. Parekh, M. M. Farid, J. R. Selman, and S. Al-Hallaj, "Solar desalination with a humidification-dehumidification technique—a comprehensive technical review," *Desalination*, vol. 160, no. 2, pp. 167–186, 2004.

[8] S. Yanniotis and K. Xerodemas, "Air humidification for seawater desalination," *Desalination*, vol. 158, no. 1, pp. 313–319, Aug. 2003.

[9] M. B. Amara, I. Houcine, and A. Guizani, "Theoretical and experimental study of a pad humidifier used in a seawater desalination process," *Desalination*, vol. 168, pp. 1–12, 2004.

[10] E. Chafik, "A new type of seawater desalination plants using solar energy," *Desalination*, vol. 156, no. 1, pp. 333–348, Aug. 2003.

[11] A. S. Cherif, S. B. Jabrallah, J.-P. Corriou, and A. Belghith, "Intensification of the liquid film evaporation in a vertical channel," *Desalination*, vol. 250, no. 1, pp. 433–437, 2010.

[12] M. Al-Shammiri, "Evaporation rate as a function of water salinity," *Desalination*, vol. 150, no. 2, pp. 189–203, 2002.

[13] G. Yuan and H. Zhang, "Mathematical modeling of a closed circulation solar desalination unit with humidification–dehumidification," *Desalination*, vol. 205, no. 1–3, pp. 156–162, 2007.

[14] G. Yuan, Z. Wang, H. Li, and X. Li, "Experimental study of a solar desalination system based on humidification–dehumidification process," *Desalination*, vol. 277, no. 1, pp. 92–98, Aug. 2011.

[15] A. M. I. Mohamed and N. A. S. El-Minshawy, "Humidification–dehumidification desalination system driven by geothermal energy," *Desalination*, vol. 249, no. 2, pp. 602–608, 2009.

[16] G. Prakash Narayan, J. H. Lienhard, and S. M. Zubair, "Entropy generation minimization of combined heat and mass transfer devices," *Int. J. Therm. Sci.*, vol. 49, no. 10, pp. 2057–2066, Oct. 2010.

[17] K. H. Mistry and S. M. Zubair, "Effect of entropy generation on the performance of humidification-dehumidification desalination cycles," *Int. J. Therm. Sci.*, vol. 49, no. 9, pp. 1837–1847, 2010.

[18] R. K. McGovern, G. P. Thiel, G. Prakash Narayan, S. M. Zubair, and J. H. Lienhard, "Performance limits of zero and single extraction humidification-dehumidification desalination systems," *Appl. Energy*, vol. 102, no. Supplement C, pp. 1081–1090, Feb. 2013.

[19] G. P. Narayan, K. M. Chehayeb, R. K. McGovern, G. P. Thiel, and S. M. Zubair, "Thermodynamic balancing of the humidification dehumidification desalination system by mass extraction and injection," *Int. J. Heat Mass Transf.*, vol. 57, no. 2, pp. 756–770, 2013.

[20] K. M. Chehayeb, G. Prakash Narayan, S. M. Zubair, and J. H. Lienhard V, "Use of multiple extractions and injections to thermodynamically balance the humidification dehumidification desalination system," *Int. J. Heat Mass Transf.*, vol. 68, pp. 422–434, Jan. 2014.

[21] G. Prakash Narayan, M. G. St. John, S. M. Zubair, and J. H. Lienhard V, "Thermal design of the humidification dehumidification desalination system: An experimental investigation," *Int. J. Heat Mass Transf.*, vol. 58, no. 1–2, pp. 740–748, Mar. 2013.

[22] R. H. Xiong, S. C. Wang, L. X. Xie, Z. Wang, and P. L. Li, "Experimental investigation of a baffled shell and tube desalination column using the humidification-dehumidification process," *Desalination*, vol. 180, no. 1–3, pp. 253–261, 2005.

[23] M. Sievers and J. H. L. V, “Design of Flat-Plate Dehumidifiers for Humidification–Dehumidification Desalination Systems,” *Heat Transf. Eng.*, vol. 34, no. 7, pp. 543–561, Jan. 2013.
[24] J. F. Klausner, Y. Li, and R. Mei, “Evaporative heat and mass transfer for the diffusion driven desalination process,” *Heat Mass Transf.*, vol. 42, no. 6, p. 528, May 2005.
[25] G. P. Narayan, M. H. Sharqawy, S. Lam, S. K. Das, and J. H. Lienhard, “Bubble columns for condensation at high concentrations of noncondensable gas: Heat-transfer model and experiments,” *AIChE J.*, vol. 59, no. 5, pp. 1780–1790, May 2013.
[26] T. Rajaseenivasan, R. K. Shanmugam, V. M. Hareesh, and K. Srithar, “Combined probation of bubble column humidification dehumidification desalination system using solar collectors,” *Energy*, vol. 116, pp. 459–469, Dec. 2016.
[27] S. A. El-Agouz, “A new process of desalination by air passing through seawater based on humidification–dehumidification process,” *Energy*, vol. 35, no. 12, pp. 5108–5114, Dec. 2010.
[28] A. Khalil, S. A. El-Agouz, Y. A. F. El-Samadony, and A. Abdo, “Solar water desalination using an air bubble column humidifier,” *Desalination*, vol. 372, pp. 7–16, Sep. 2015.
[29] Z. Zeng, A. Sadeghpour, and Y. S. Ju, “Thermohydraulic characteristics of a multi-string direct-contact heat exchanger,” *Int. J. Heat Mass Transf.*, vol. 126, Part A, pp. 536–544, Nov. 2018.
[30] Z. Zeng, A. Sadeghpour, G. Warrier, and Y. S. Ju, “Experimental study of heat transfer between thin liquid films flowing down a vertical string in the Rayleigh-Plateau instability regime and a counterflowing gas stream,” *Int. J. Heat Mass Transf.*, vol. 108, Part A, pp. 830–840, May 2017.
[31] H. Migita, K. Soga, and Y. H. Mori, “Gas absorption in a wetted-wire column,” *AIChE J.*, vol. 51, no. 8, pp. 2190–2198, Aug. 2005.
[32] S. G. Pakdehi and S. Taheri, “Separation of Hydrazine from Air by Wetted Wire Column,” *Chem. Eng. Technol.*, vol. 33, no. 10, pp. 1687–1694, Oct. 2010.
[33] S. A. Galledari, R. Alizadeh, E. Fatehifar, and E. Soroush, “Simulation of carbon dioxide absorption by monoethanolamine solution in wetted-wire column,” *Chem. Eng. Process. Process Intensif.*, vol. 102, pp. 59–69, 2016.
[34] A. Sadeghpour, Z. Zeng, and Y. S. Ju, “Effects of Nozzle Geometry on the Fluid Dynamics of Thin Liquid Films Flowing down Vertical Strings in the Rayleigh–Plateau Regime,” *Langmuir*, vol. 33, no. 25, pp. 6292–6299, Jun. 2017.
[35] A. F. Mills, *Mass Transfer*, 1 edition. Upper Saddle River, N.J: Prentice Hall, 2001.
[36] T. L. Bergman, F. P. Incropera, D. P. DeWitt, and A. S. Lavine, *Fundamentals of Heat and Mass Transfer*. John Wiley & Sons, 2011.
[37] R. W. Hyland and A. Wexler, “Formulations for the thermodynamic properties of dry air from 173.15 to 473.15 K, at pressure to 5 MPa,” *ASHRAE Trans*, vol. 89, pp. 520–535, 1983.
[38] W. Wagner and A. Pruss, “The IAPWS formulation 1995 for the thermodynamic properties of ordinary water substance for general and scientific use,” *J. Phys. Chem. Ref. Data*, vol. 31, no. 2, pp. 387–535, 2002.
[39] M. H. Sharqawy, J. H. Lienhard, and S. M. Zubair, “Thermophysical properties of seawater: a review of existing correlations and data,” *Desalination Water Treat.*, vol. 16, no. 1–3, pp. 354–380, 2010.
[40] K. S. Spiegler, *Principles of desalination*. Elsevier, 2012.
[41] K.-C. Park *et al.*, “Condensation on slippery asymmetric bumps,” *Nature*, vol. 531, no. 7592, p. 78, 2016.
[42] C. Duprat, C. Ruyer-Quil, and F. Giorgiutti-Dauphiné, “Spatial evolution of a film flowing down a fiber,” *Phys. Fluids 1994-Present*, vol. 21, no. 4, p. 042109, Apr. 2009.
[43] G. P. Narayan, K. H. Mistry, M. H. Sharqawy, S. M. Zubair, and J. H. Lienhard, “Energy effectiveness of simultaneous heat and mass exchange devices,” *Glob. Digit. Cent.*, 2010.
[44] K. Rehme, “Pressure drop performance of rod bundles in hexagonal arrangements,” *Int. J. Heat Mass Transf.*, vol. 15, no. 12, pp. 2499–2517, 1972.
[45] K. Rehme, “Simple method of predicting friction factors of turbulent flow in non-circular channels,” *Int. J. Heat Mass Transf.*, vol. 16, no. 5, pp. 933–950, 1973.
[46] K. Rehme and G. Trippe, “Pressure drop and velocity distribution in rod bundles with spacer grids,” *Nucl. Eng. Des.*, vol. 62, no. 1–3, pp. 349–359, 1980.
[47] J. Nikuradse, “Gesetzmäßigkeiten der turbulenten Strömung in glatten Rohren,” *Forsch. Im Ingenieurwesen*, vol. 4, no. 1, pp. 44–44, 1933.
[48] K. Maubach, “Reibungsgesetze turbulenter strömungen,” *Chem. Ing. Tech.*, vol. 42, no. 15, pp. 995–1004, 1970.
[49] E. M. Sparrow and A. L. Loeffler, “Longitudinal laminar flow between cylinders arranged in regular array,” *AIChE J.*, vol. 5, no. 3, pp. 325–330, Sep. 1959.